Materials Advances

ROYAL SOCIETY OF CHEMISTRY

PAPER

View Article Online
View Journal | View Issue

Cite this: *Mater. Adv.*, 2022, 3, 3267

Improving the temperature-sensing performance of the $SrZn_{0.33}Nb_{0.67}O_3:Pr^{3+}$ phosphor *via* Ga^{3+} doping†

Yan Cui, Yan Gao,* Zhichao Meng, Tao Hu, Yeqing Chen, Yan Chen and Qingguang Zeng*

Received 27th December 2021,
Accepted 21st February 2022

DOI: 10.1039/d1ma01247a

rsc.li/materials-advances

Optical thermometry offers promising applications in the fields of microelectronics and biomedicine, as well as in fire pre-warning systems. In this research, Pr^{3+}-activated $SrZn_{0.33}Nb_{0.67}O_3$ phosphors were successfully prepared *via* solid-state reactions. Under ultraviolet excitation, the $SrZn_{0.33}Nb_{0.67}O_3:x\%Pr^{3+}$ (x = 0.25/0.75/1.25/2) phosphors exhibit bright blue and red emissions, located at 491 nm ($^3P_0 \rightarrow {}^3H_4$), 619 nm ($^1D_2 \rightarrow {}^3H_4$) and 651 nm ($^3P_0 \rightarrow {}^3F_2$). Specifically, two fluorescence intensity ratio (FIR) models of $^1D_2 \rightarrow {}^3H_4$ *versus* $^3P_0 \rightarrow {}^3H_4$ (Red1/Blue) and $^1D_2 \rightarrow {}^3H_4$ *versus* $^3P_0 \rightarrow {}^3F_2$ (Red1/Red2) in the temperature range of 300–500 K are adopted for temperature sensing. Our results show that the designed phosphor can serve as a novel potential self-calibrated optical thermometer. Moreover, the temperature sensitivity of the FIR thermometer is significantly enhanced when Ga^{3+} is incorporated into the $SrZn_{0.33}Nb_{0.67}O_3$. Specifically, the maximum absolute and relative sensitivity for the 6% Ga^{3+} co-doped sample are increased five- and two-fold, respectively, compared with the undoped sample. This work may provide useful inspiration for effectively improving the temperature-sensing performance of optical thermometers.

Introduction

With rapid developments in the microelectronics industry, biomedical field and scientific research, accurate temperature information acquisition with high spatio-temporal resolution has been gaining greater importance. Compared with traditional mercury-in-glass thermometers and thermocouples, rare-earth-doped non-contact optical thermometers are becoming more and more popular for temperature measurements in harsh environments, such as in corrosive liquids and in environments with electromagnetic interference.[1–4] Generally, the emission intensity/bandwidth, peak position, fluorescence intensity ratio (FIR) and lifetime of the luminescence center can all be used as indexes for temperature monitoring.[5] Among these, the FIR technique has wide-ranging advantages due to its ease of operation, fast response and high reliability.[6–9]

Over the past decades, most of the studies based on FIR thermometry have focused on Er^{3+}-doped up-conversion temperature-sensing materials that have two closely spaced temperature-sensitive thermally coupled levels ($^2H_{11/2}$, and $^4S_{3/2}$).[10–12] However, the narrow energy gap of the thermally coupled levels results in poor signal discrimination. Other luminescent materials, such as fluorescein dye, carbon dots, quantum dots, *etc.*, have also been investigated for FIR thermometry.[13–15] However, these materials are usually vulnerable to the physical and chemical environments, which restricts their practical application. Currently, the temperature-sensing strategy based on the diverse temperature responses of 4f–5d or 4f–4f transitions of Pr^{3+} is attracting much attention for its high signal discrimination and considerable temperature sensitivity.[16–20] Pr^{3+} has abundant emission spectral lines, where blue, green, red and deep red emissions are derived from the $^3P_0 \rightarrow {}^3H_4$, $^3P_{1,0} \rightarrow {}^3H_5$, $^1D_2 \rightarrow {}^3H_4$ and $^3P_0 \rightarrow {}^3F_2$ electronic transitions, respectively. Among these, the blue and red emissions that stem from the $^3P_0$ and $^1D_2$ states are usually used as signal peaks for research in FIR thermometry. As is known, influences from phonon-assisted cross-relaxation, multiphonon relaxation and the intervalence charge transfer state (IVCT) mean that the intensity ratio of these transitions is very vulnerable to temperature in some transition metal oxides. For example, Pr^{3+}-doped $(K_{0.5}Na_{0.5})NbO_3$, La_2MgTiO_6, $Na_2La_2Ti_3O_{10}$ and $LaMg_{0.402}Nb_{0.598}O_3$ have been reported as potential optical thermometers.[21–24] It is worth noting that IVCT-affected thermal-quenching process is the key factor that contributes

School of Applied Physics and Materials, Wuyi University, Jiangmen 529020, Guangdong Province, P. R. China. E-mail: gaoyan_chn@sina.com, zengqg@mail.ustc.edu.cn

† Electronic supplementary information (ESI) available. See DOI: 10.1039/d1ma01247a

to the excellent temperature-sensing performance. Hence, choosing a suitable host and regulating the IVCT band are effective ways to achieve a high temperature-sensing performance.

The complex perovskite compound $SrZn_{0.33}Nb_{0.67}O_3$ has drawn our attention. This compound belongs to the $A_3B'B''_2O_9$ family in which the A-sites are occupied by larger cations and the B-sites by smaller cations. The abundant lattice sites, wide spectral excitation and excellent chemical stability make it a suitable matrix for developing rare-earth luminescent materials.[25–27] To the best of our knowledge, the thermo-sensitive properties of the $SrZn_{0.33}Nb_{0.67}O_3:Pr^{3+}$ phosphor have not been systematically investigated so far. Therefore, a study on the temperature-dependent luminescent properties of Pr^{3+} in $SrZn_{0.33}Nb_{0.67}O_3$ will broaden the family of potential Pr^{3+}-activated optical thermometers. In addition, co-doping with other ions is an effective way to achieve enhancement of the temperature-sensing performance.[28–30] For example, the green up-conversion emission and thermal sensitivity of $NaYF_4$: Yb,Er^{3+} are both increased when Ga^{3+} is introduced into the host.[31] The luminescent intensity of $CaAl_{12}O_{19}:Mn^{4+}$ is enhanced *via* Ga^{3+} doping.[32] The thermal stability and red emission of Mn^{4+} in Li_2MgZrO_4 are improved when Ga^{3+} ions are incorporated into the phosphor.[33] The above studies indicate a practicable strategy for us to promote the performance of Pr^{3+}-activated self-calibrated optical thermometers.

Thus, in this work, we chose to study a novel Pr^{3+}-activated $SrZn_{0.33}Nb_{0.67}O_3$ thermo-sensitive phosphor and investigate the significant impact of Ga^{3+} co-doping on the temperature-sensing performance of this material. Herein, the $SrZn_{0.33}Nb_{0.67}O_3:x\%Pr^{3+}$ (x = 0.25/0.75/1.25/2) phosphors were successfully prepared using a high-temperature solid-state method, and the impact of the Pr^{3+} concentration on the luminescence properties is discussed. Under ultraviolet excitation, the as-synthesized samples exhibit efficient blue and red emissions located at 491 nm ($^3P_0 \rightarrow {}^3H_4$), 619 nm ($^1D_2 \rightarrow {}^3H_4$) and 651 nm ($^3P_0 \rightarrow {}^3F_2$), and the FIR of different 4f configuration transitions changes significantly with temperature, demonstrating that the studied material can serve as a self-calibrated optical thermometer with good signal discrimination. Specifically, two FIR models of $^1D_2 \rightarrow {}^3H_4$ *versus* $^3P_0 \rightarrow {}^3H_4$ (Red1/Blue) and $^1D_2 \rightarrow {}^3H_4$ *versus* $^3P_0 \rightarrow {}^3F_2$ (Red1/Red2) in the temperature range of 300–500 K are adopted for temperature sensing. Notably, the temperature-sensing performance of the thermometer is improved markedly when Ga^{3+} is co-doped into the $SrZn_{0.33}Nb_{0.67}O_3:Pr^{3+}$ phosphor. It is hoped that the designed phosphor will be a potential candidate for applications in optical thermometry.

Experimental

Synthesis

The $SrZn_{0.33}Nb_{0.67}O_3:x\%\,Pr^{3+},y\%\,Ga^{3+}$($x$ = 0.25/0.75/1.25/2; y = 4/6/8) samples were synthesized using the high-temperature solid-state method. The strontium carbonate ($SrCO_3$), zinc oxide (ZnO), niobium oxide (Nb_2O_5), praseodymium oxide (Pr_6O_{11}), and gallium oxide (Ga_2O_3) used in the experiments were purchased from the Aladdin Reagent Company. In a typical synthesis, stoichiometric amounts of $SrCO_3$, Nb_2O_5, ZnO, Pr_6O_{11}, and Ga_2O_3 were mixed thoroughly and ground with flux using ethanol as a wetting agent, placed in a corundum crucible and heated at 800 °C for 2 h in air. After cooling to room temperature, the powder was ground and calcined at 1350 °C for 8 h in air.

Characterization

The X-ray diffraction (XRD) patterns were collected using a powder diffractometer with Cu Kα radiation (λ = 1.5418 Å). A scanning electron microscope (SEM, JSM-6700F) was used to characterize the morphology, energy dispersive X-ray spectroscopy (EDS) and elemental mapping of the samples. Diffuse reflectance spectra were recorded using a UV-Vis-NIR spectrophotometer (Lambda 950, PerkinElmer). An FLS 980 fluorescence spectrometer with a 450 W xenon lamp as the excitation light source was used to measure the photoluminescence excitation (PLE) and photoluminescence emission (PL) spectra and the fluorescence decay curves of the samples. Temperature-dependent PL spectra were measured using the above-mentioned spectrophotometer, which was equipped with a temperature-controlling stage.

Results and discussion

Fig. 1(a) shows the XRD patterns of $SrZn_{0.33}Nb_{0.67}O_3:x\%$ $Pr^{3+},y\%$ Ga^{3+} (x = 0/0.25/0.75/1.25/2; y = 4/6/8). All the diffraction peaks can be well indexed to the standard PDF card (no. 39-1470) with no impurity peaks observed, which confirms that the synthesized samples are of pure phase. The doping of Pr^{3+} and Ga^{3+} ions did not change the crystal structure of $SrZn_{0.33}Nb_{0.67}O_3$. When Pr^{3+} and Ga^{3+} ions are incorporated into $SrZn_{0.33}Nb_{0.67}O_3$, the position of the diffraction peaks shifts to the larger-angle side, as exhibited in Fig. 1(a) for the strongest line located at 31.6°. Fig. 1(b) presents the crystal structure of $SrZn_{0.33}Nb_{0.67}O_3$, which belongs to the cubic perovskite structure in the space group $Fm\bar{3}m$. Zn and Nb atoms are disorderly distributed at the B site, coordinated with 6 oxygen atoms to form [Zn/NbO_6] octahedra, while the Sr^{2+} ion is located at the A site with 12-fold coordinated oxygen. Due to the similar ionic radii of Pr^{3+} and Sr^{2+} ($r_{Pr^{3+}}$ = 1.29 Å for CN = 12, $r_{Sr^{2+}}$ = 1.44 Å for CN = 12), Pr^{3+} should substitute for the Sr^{2+} ion. By contrast, the ionic radius of Ga^{3+} ($r_{Ga^{3+}}$ = 0.62 Å, CN = 6) is similar to that of the Nb^{5+} and Zn^{2+} ions ($r_{Zn^{2+}}$ = 0.74 Å, $r_{Nb^{5+}}$ = 0.64 Å for CN = 6), so the Ga^{3+} ion should occupy the Zn^{2+}/Nb^{5+} site. SEM and elemental map observations, as displayed in Fig. 1(c–j), show that the as-prepared $SrZn_{0.33}Nb_{0.67}O_3$:6% Ga^{3+},1.25% Pr^{3+} powder has a small particle size below 5 μm, and the Sr, Zn, Nb, O and Ga elements are homogeneously distributed throughout the observation area. Moreover, the peaks of the Sr, Zn, Nb, O and Ga elements all

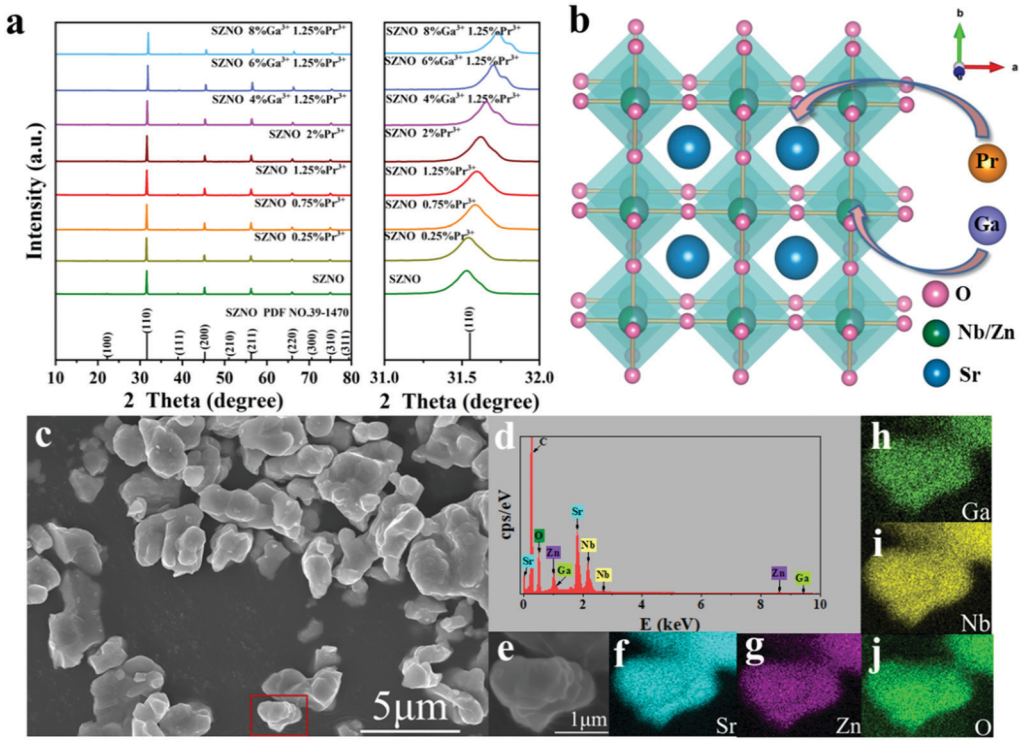

Fig. 1 (a) XRD patterns of $SrZn_{0.33}Nb_{0.67}O_3$:*x*% Pr^{3+},*y*% Ga^{3+} (*x* = 0/0.25/0.75/1.25/2; *y* = 4/6/8), referenced to the $SrZn_{0.33}Nb_{0.67}O_3$ (PDF no. 39-1470) standard card. Magnification of patterns in the 31–32° range are on the right. (b) Schematic diagram of the $SrZn_{0.33}Nb_{0.67}O_3$ crystal structure. (c) SEM image, (d) EDS spectrum and (e–j) elemental mapping images of $SrZn_{0.33}Nb_{0.67}O_3$:1.25% Pr^{3+},6% Ga^{3+}.

appear in the EDS energy spectrum, further proving the successful incorporation of Ga^{3+} ions into niobate matrix.

Fig. 2(a) shows the room-temperature PL spectra of the $SrZn_{0.33}Nb_{0.67}O_3$ phosphors doped with different Pr^{3+}-ion concentrations. It is found that under the excitation of 290 nm UV light, the as-prepared $SrZn_{0.33}Nb_{0.67}O_3$:*x*% Pr^{3+} (*x* = 0.25/0.75/1.25/2) samples exhibit three main emission peaks at 491 nm, 619 nm and 651 nm, which correspond to the $^3P_0 \rightarrow {}^3H_4$, $^1D_2 \rightarrow {}^3H_4$ and $^3P_0 \rightarrow {}^3F_2$ transitions of Pr^{3+}, respectively. The emission intensity of the three emission peaks (491 nm, 619 nm and 651 nm) have similar line trends with the Pr^{3+} doping concentration. When the Pr^{3+} doping concentration was increased from 0.25% to 2%, the emission intensities of the peaks were all gradually increased, and any further increase in the doping concentration resulted in a lowered emission intensity due to concentration quenching; therefore, the optimal Pr^{3+} doping concentration is 1.25%. In order to investigate the energy-transfer mechanism of Pr^{3+} in the $SrZn_{0.33}Nb_{0.67}O_3$ host, the critical distance R_c is calculated using the following equation,[34]

$$R_c \approx 2\left[\frac{3V}{4\pi x_c N}\right]^{\frac{1}{3}} \quad (1)$$

where V is the unit cell volume, x_c is the critical doping concentration, and N represents the number of lattice sites in the unit that can be occupied by activator ions. For $SrZn_{0.33}Nb_{0.67}O_3$:Pr^{3+}, V = 64.1 Å^3, x_c = 1.25, N = 2, and R_c was calculated to be 3.68 Å; thus, the electric exchange interaction is responsible for the non-radiative energy transfer in $SrZn_{0.33}Nb_{0.67}O_3$.

Fig. 2(b) exhibits the fluorescence decay curves measured at the 491 nm ($^3P_0 \rightarrow {}^3H_4$), 619 nm ($^1D_2 \rightarrow {}^3H_4$), and 651 nm ($^3P_0 \rightarrow {}^3F_2$) emissions for $SrZn_{0.33}Nb_{0.67}O_3$:1.25% Pr^{3+}. All curves exhibit triple-exponential decay behaviour, and can be fitted using the following formula,[35]

$$I(t) = B_1 \exp\left(-\frac{t}{\tau_1}\right) + B_2 \exp\left(-\frac{t}{\tau_2}\right) + B_3 \exp\left(-\frac{t}{\tau_3}\right) \quad (2)$$

where $I(t)$ is the fluorescence intensity of the emission peak monitored at time t; B_1, B_2 and B_3 are constants, and τ_1, τ_2 and τ_3 are the lifetimes of each exponential component. The deviation from single-exponential decay is due to the existence of several de-excitation pathways including the radiative transition, cross-relaxation (CR) and multiphonon relaxation (MPR) processes as well as the intervalence charge transfer state (IVCT). The average lifetime (τ) can be calculated:

$$\tau = \frac{B_1\tau_1^2 + B_2\tau_2^2 + B_3\tau_3^2}{B_1\tau_1 + B_2\tau_2 + B_3\tau_3} \quad (3)$$

Finally, the fluorescence decay lifetime of the $^1D_2$ energy level by *via* monitoring at the 619 nm emission is 20.51 μs, and the decay lifetime of the $^3P_0$ level by monitoring at the 491 nm and 651 nm emissions are calculated as 9.29 μs and 8.47 μs, respectively. Due to its spin-allowed transition characteristics, the excited electrons at the $^3P_0$ energy level decay much faster

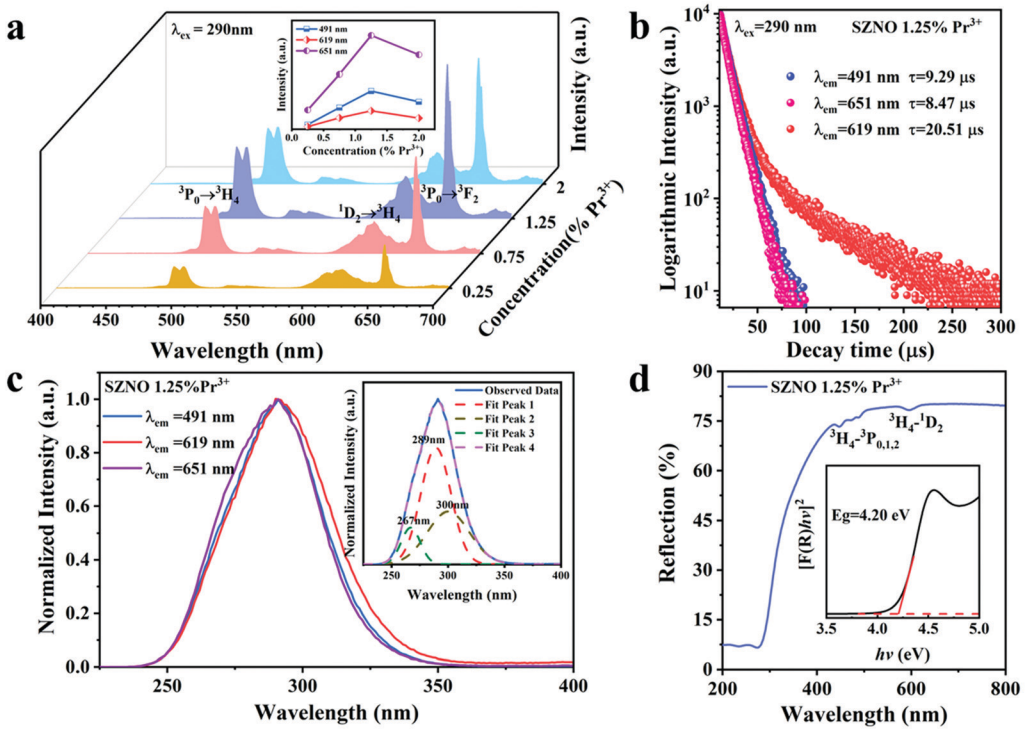

Fig. 2 (a) PL spectra of $SrZn_{0.33}Nb_{0.67}O_3$:*x*% Pr^{3+} (*x* = 0.25/0.75/1.25/2) at room temperature. The inset shows a comparison of the emission intensity for the 491 nm, 619 nm and 651 nm peaks for different Pr^{3+}-ion concentrations. (b) Fluorescence decay curves and (c) excitation spectra (λ_{em} = 491 nm, 619 nm, and 651 nm) for $SrZn_{0.33}Nb_{0.67}O_3$:1.25% Pr^{3+}. (d) ultraviolet visible diffuse reflectance spectra (UV vis DRS) of the $SrZn_{0.33}Nb_{0.67}O_3$:1.25% Pr^{3+}, where the inset shows the relationship of $[F(R)h\nu]^2$ *versus* the energy $h\nu$.

than at the $^1D_2$ energy level. Fig. 2(c) shows the normal temperature PLE spectra of $SrZn_{0.33}Nb_{0.67}O_3$:1.25% Pr^{3+} measured by monitoring the emission peaks at λ_{em} = 491 nm, 619 nm, and 651 nm. It is found that all the excitation spectra are similar, and the maximum excitation wavelength is around 290 nm. The inset of Fig. 2(c) shows the Gaussian fitting result of one typical PLE spectrum, where the three Gaussian deconvolution peaks at 267 nm, 289 nm and 300 nm are suggested to be assigned to the $4f^2 \rightarrow 4f5d$ transition of Pr^{3+}, the host absorption and Pr^{3+}–Nb^{5+} IVCT. From the diffuse reflectance spectra of the $SrZn_{0.33}Nb_{0.67}O_3$ host and $SrZn_{0.33}Nb_{0.67}O_3$:1.25% Pr^{3+} displayed in Fig. S1 (ESI†) and Fig. 2(d), respectively, both show a strong host absorption in the 200–400 nm UV region. Besides the host fundamental absorption, there also exist several absorption dips in the 450–500 nm and 580–625 nm regions of $SrZn_{0.33}Nb_{0.67}O_3$:1.25% Pr^{3+}, which originate from the 4f–4f intra-configuration transitions of the Pr^{3+} ion, *i.e.*, the $^3H_4$–$^3P_{0,1,2}$ and the $^3H_4$–$^1D_2$ transition, respectively. Due to the parity-forbidden transition nature, their absorptions are very weak. According to the Tauc theoretical equation, the optical band gap of $SrZn_{0.33}Nb_{0.67}O_3$ can be calculated using the following formula:

$$[F(R)h\nu]^n = A(h\nu - E_g) \quad (4)$$

$$[F(R)] = (1 - R)^2/2R \quad (5)$$

where h is the Planck constant, ν is the incident photon frequency, A and E_g are the proportional constant and the optical band gap energy, n is related to the transition type, *i.e.*, n = 1/2 for an indirect transition, and n = 2 for a direct transition, and R is the reflection coefficient. In the $SrZn_{0.33}Nb_{0.67}O_3$ host, the value of n should be 2 due to it is direct bandgap.[25] The inset of Fig. 2(d) shows the function relationship between $[F(R)h\nu]^2$ and $h\nu$ for $SrZn_{0.33}Nb_{0.67}O_3$:1.25% Pr^{3+}. The optical band gaps of the $SrZn_{0.33}Nb_{0.67}O_3$ host and $SrZn_{0.33}Nb_{0.67}O_3$:1.25% Pr^{3+} were calculated to be about 4.20 eV.

Next, temperature-dependent photoluminescence spectrum testing was performed on $SrZn_{0.33}Nb_{0.67}O_3$:1.25% Pr^{3+} to investigate its potential applications in temperature sensing. As shown in Fig. 3(a), with the temperature increasing from 300–500 K, the intensity of the blue emission at 491 nm ($^3P_0 \rightarrow {}^3H_4$) and the red emission at 651 nm ($^3P_0 \rightarrow {}^3F_2$) drop dramatically, whereas the red emission at 619 nm ($^1D_2 \rightarrow {}^3H_4$) shows insignificant quenching (Fig. 3b–d). Significantly, the FIR of $^1D_2 \rightarrow {}^3H_4$ and $^3P_0 \rightarrow {}^3H_4$ (Red1/Blue), as well as $^1D_2 \rightarrow {}^3H_4$ and $^3P_0 \rightarrow {}^3F_2$ (Red1/Red2) could be used as detection signals for temperature monitoring. The FIR *versus* $1/T$ plots for $SrZn_{0.33}Nb_{0.67}O_3$:1.25% Pr^{3+} are presented in Fig. 4(a and b). It can be seen that the FIR for the two models changes clearly with increasing temperature. The FIR can be expressed as follows:[36]

$$\mathrm{FIR} \approx C + A \exp(-B/k_B T) \quad (6)$$

where k_B is the Boltzmann constant, T is the temperature, and A, B and C are constants. Since sensitivity is a very important

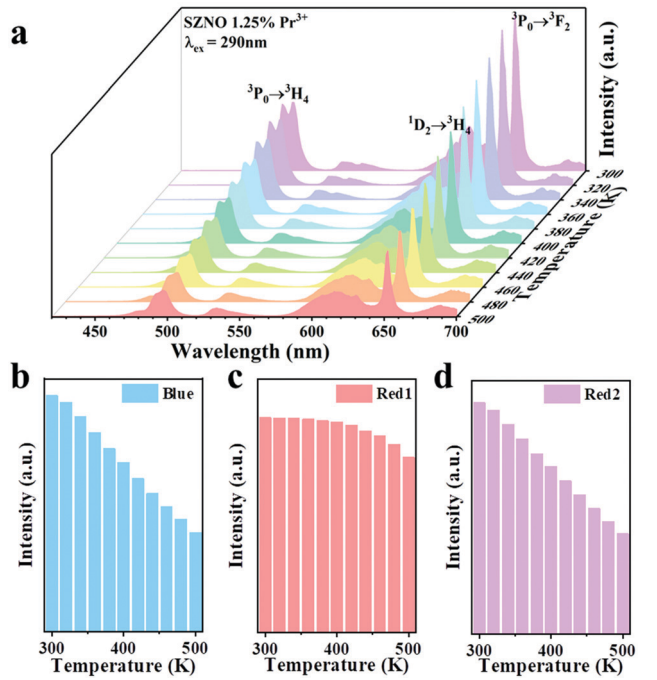

Fig. 3 (a) Temperature-dependent PL spectra of the $SrZn_{0.33}Nb_{0.67}O_3$:1.25% Pr^{3+} sample, recorded from 300 K to 500 K. (b), (c) and (d) Histograms displaying the luminescence intensity of the 491 nm, 619 nm and 651 nm peaks at different temperatures for the $SrZn_{0.33}Nb_{0.67}O_3$:1.25% Pr^{3+} sample.

working parameter for temperature sensors, in order to quantitatively assess the thermo-sensitive properties of the phosphor, the absolute temperature sensitivity (S_a) and the relative temperature sensitivity (S_r) were calculated using the following equations:[36]

$$S_a = \left|\frac{\delta \mathrm{FIR}}{\delta T}\right| = A\exp\left(-\frac{B}{k_B T}\right) \times \frac{B}{k_B T^2} \quad (7)$$

$$S_r = \left|\frac{1}{\mathrm{FIR}}\frac{\delta \mathrm{FIR}}{\delta T}\right| \times 100\% \quad (8)$$

The relationship between T and the absolute sensitivity S_a as well as the relative sensitivity S_r are shown in Fig. 4(c and d). The maximum values of S_a and S_r for $SrZn_{0.33}Nb_{0.67}O_3$:1.25% Pr^{3+} were calculated to be 0.007 K^{-1} (500 K) and 0.37% K^{-1} (400 K), respectively. The above results demonstrate that the as-prepared phosphor is a new potential thermo-sensitive material.

To further improve the temperature-sensing characteristics of $SrZn_{0.33}Nb_{0.67}O_3$:1.25% Pr^{3+},y% Ga^{3+} (y = 4/6/8) ions were incorporated into the $SrZn_{0.33}Nb_{0.67}O_3$ matrix. Fig. 5(a and c) shows the PL and PLE spectra of $SrZn_{0.33}Nb_{0.67}O_3$:1.25% Pr^{3+},6% Ga^{3+} (the PL and PLE spectra for Ga^{3+}-ion-doping concentrations of 4% and 8% are presented in Fig. S2, ESI†). The emission peaks are similar to those of $SrZn_{0.33}Nb_{0.67}O_3$:1.25% Pr^{3+} while the excitation bands shift towards a low energy for the 6% Ga^{3+}-doped sample monitored at 491 nm, 619 nm and 651 nm. The smaller band gap determined *via* the diffuse reflectance spectrum for $SrZn_{0.33}Nb_{0.67}O_3$:6% Ga^{3+},1.25% Pr^{3+} in Fig. 5(d) corroborates the changes mentioned above. The band gaps are reduced as

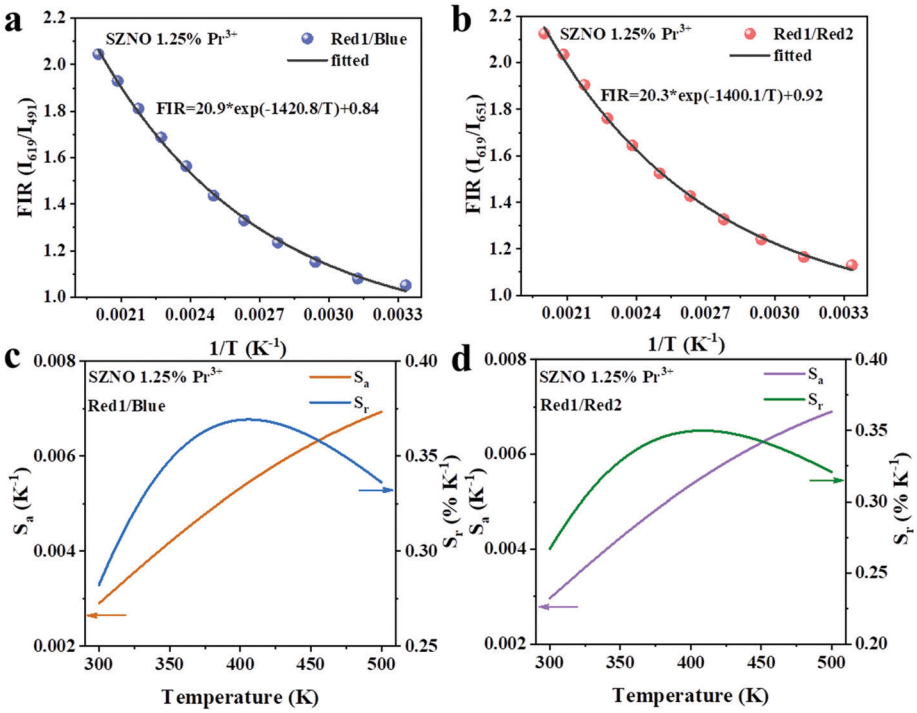

Fig. 4 Experimentally measured and eqn (6)-fitted plots of (a) FIR (I_{619}/I_{491}) and (b) FIR (I_{619}/I_{651}) *versus* temperature. The measured and calculated plots of S_a and S_r *versus* temperature based on (c) FIR (I_{619}/I_{491}) and (d) FIR (I_{619}/I_{651}) models.

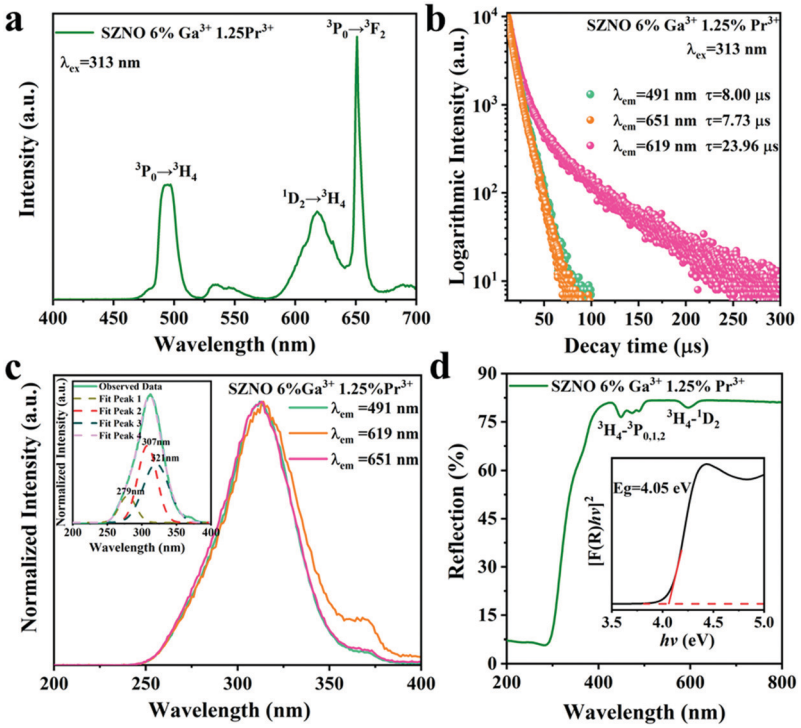

Fig. 5 (a) PL spectra, (b) fluorescence decay curves, (c) PLE spectra (λ_{em} = 491 nm, 619 nm, 651 nm) and (d) the UV-vis DRS of the $SrZn_{0.33}Nb_{0.67}O_3$:6% Ga^{3+},1.25% Pr^{3+}, where the inset in (c) shows the Gaussian fitting performed on the excitation spectra, the inset in (d) shows the relationship of $[F(R)h\nu]^2$ *versus* energy $h\nu$.

well when different concentrations of Ga^{3+} ions were introduced into the matrix (Fig. S3, ESI†). In addition, the fluorescence intensity ratio of red light ($^1D_2 \rightarrow {}^3H_4$) and blue light ($^3P_0 \rightarrow {}^3H_4$) increased after Ga^{3+} doping, as demonstrated in Fig. 5(a), and to further understand this, the excited dynamics of the $^1D_2$ and $^3P_0$ energy levels were also investigated. Fig. 5(b) shows the fluorescence decay curves of $SrZn_{0.33}Nb_{0.67}O_3$:6% Ga^{3+},1.25% Pr^{3+}. The calculated fluorescence decay lifetime for the $^1D_2$ energy level is 23.96 μs (619 nm, $^1D_2 \rightarrow {}^3H_4$), which is longer than that measured in $SrZn_{0.33}Nb_{0.67}O_3$:1.25% Pr^{3+}, while the fluorescence decay rate of the $^3P_0$ state is accelerated slightly, resulting in a shorter decay time of the $^3P_0$ energy level. These results suggest that Ga^{3+} doping can enhance the non-radiative transition possibility of the $^3P_0$ state. At ambient temperature, the effect of multiphonon relaxation (MPR) is negligible. Therefore, the decay deviation could be mainly caused by cross-relaxation (CR) [$^3P_0$, $^3H_4$] → [$^1D_2$, $^3H_6$] and crossover to IVCT.

Subsequently, the temperature-dependent spectra of the phosphors with different Ga^{3+} doping concentrations (4%, 6%, and 8%) were investigated. The temperature-dependent PL spectra of $SrZn_{0.33}Nb_{0.67}O_3$:y% Ga^{3+},1.25% Pr^{3+} (y = 4/6/8) are shown in Fig. 6(a, c and d). It is demonstrated in Fig. 6(b) that the intensity of the $^3P_0 \rightarrow {}^3H_4$ and $^3P_0 \rightarrow {}^3H_2$ emissions drop more with increasing temperature after co-doping with Ga^{3+} ions. As a consequence, compared with $SrZn_{0.33}Nb_{0.67}O_3$:1.25% Pr^{3+}, the thermal response of Red1/Blue and Red1/Red2 for the Ga^{3+} co-doped samples behave more dramatically. With the increase in temperature, the FIR value of Red1/Blue varies over 1.13–2.04 for $SrZn_{0.33}Nb_{0.67}O_3$:1.25% Pr^{3+}, while it is 1.36–4.23 for the 6% Ga^{3+}-doped sample. Similarly, the FIR value of Red1/Red2 varies over 1.13–2.13 for $SrZn_{0.33}Nb_{0.67}O_3$:1.25% Pr^{3+}, while it is 1.57–4.14 for the 6% Ga^{3+}-doped sample (Fig. S4, ESI†).

The absolute sensitivity S_a and the relative sensitivity S_r curves calculated using eqn (5) and (6) for the Ga^{3+},Pr^{3+} co-doped $SrZn_{0.33}Nb_{0.67}O_3$ phosphors are shown in Fig. 7, and the maximum S_a and S_r values are also shown in Table 1. Clearly, in comparison with the Pr^{3+} single-doped $SrZn_{0.33}Nb_{0.67}O_3$ phosphor, S_a and S_r are both significantly increased to some degree for the 4%, 6% and 8% Ga^{3+} co-doped phosphors. Remarkably, the maximal S_a and S_r values reach as high as 0.035 K^{-1} (500K) and 0.83% K^{-1} (500 K) for the 6% Ga^{3+} co-doped sample, which are increased by five- and two-fold, respectively, compared with the undoped sample. All these demonstrate that co-doping with Ga^{3+} ions effectively improves the performance of the $SrZn_{0.33}Nb_{0.67}O_3$:Pr^{3+} thermo-sensitive phosphor.

According to the above results, the markedly improved temperature-sensing performance is caused directly by the more significant thermal quenching of the $^3P_0$ state after Ga^{3+} co-doping. To further understand the fluorescence quenching dynamics, the possible depopulation process for the $^3P_0$ state was discussed. As observed in Fig. 8, three de-excitation modes may contribute to the thermal quenching of the $^3P_0$-related luminescence, namely, phonon-assisted cross-relaxation(CR), multiphonon relaxation (MPR) and crossover to a low-lying

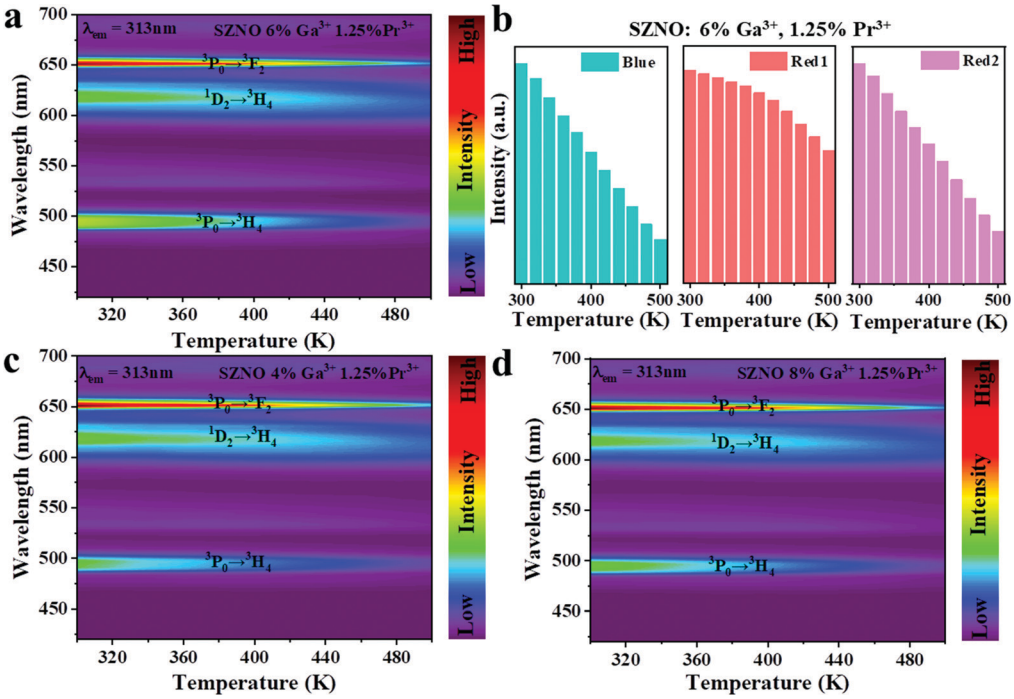

Fig. 6 (a) Temperature-dependent PL spectra of the $SrZn_{0.33}Nb_{0.67}O_3$:6% Ga^{3+},1.25% Pr^{3+}, recorded from 300 K to 500 K. (b) Histograms displaying the luminescence intensity of the 491 nm (Blue), 619 nm (Red1) and 651 nm (Red2) peaks at different temperatures for the $SrZn_{0.33}Nb_{0.67}O_3$:6% Ga^{3+},1.25% Pr^{3+}. (c) Temperature dependent PL spectra of the $SrZn_{0.33}Nb_{0.67}O_3$:4% Ga^{3+},1.25% Pr^{3+} and (d) $SrZn_{0.33}Nb_{0.67}O_3$:8% Ga^{3+},1.25% Pr^{3+}, recorded from 300 K to 500 K.

IVCT state. Considering that the CR processes of [$^3P_0$, $^3H_4$][$^1G_4$, $^1G_4$] and [$^3P_0$, $^3H_4$][$^1D_2$, $^3H_6$] are non-resonant, whereas the [$^1D_2$, $^3H_4$][$^1G_4$, $^3F_4$] is resonant, as a consequence, the probability of the phonon-involved former CR processes is more

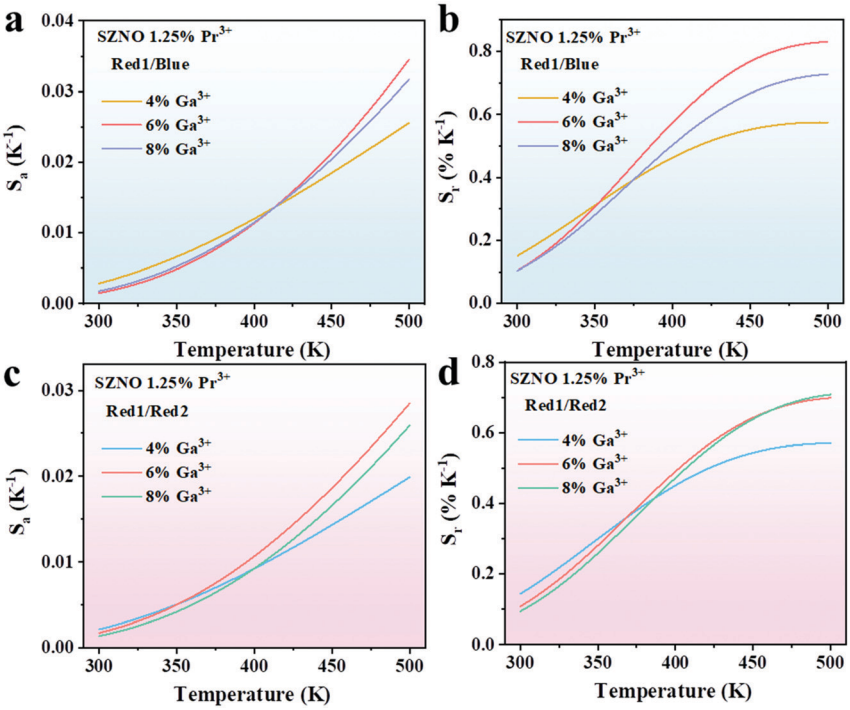

Fig. 7 (a) Absolute sensitivity S_a and (b) relative sensitivity S_r *versus* temperature for the Red1/Blue model for $SrZn_{0.33}Nb_{0.67}O_3$:*y*% Ga^{3+},1.25% Pr^{3+} (*y* = 4/6/8). (c) Absolute sensitivity S_a and (d) relative sensitivity S_r *versus* temperature for the Red1/Red2 model for $SrZn_{0.33}Nb_{0.67}O_3$:*y*% Ga^{3+},1.25% Pr^{3+} (*y* = 4/6/8).

Table 1 Calculated maximum S_a and S_r values of $SrZn_{0.33}Nb_{0.67}O_3$:y% Ga^{3+},1.25% Pr^{3+} (y = 4/6/8)

Transition	Material	Temperature range (K)	$S_{a\text{-}max}$ (K^{-1})	$S_{r\text{-}max}$ (% K^{-1})
Pr^{3+}: $^1D_2 \rightarrow {}^3H_4$, $^3P_0 \rightarrow {}^3H_4$	$SrZn_{0.33}Nb_{0.67}O_3$	300–500	0.007 (500 K)	0.37 (400 K)
	$SrZn_{0.33}Nb_{0.67}O_3$:4% Ga^{3+}	300–500	0.026 (500 K)	0.58 (500 K)
	$SrZn_{0.33}Nb_{0.67}O_3$:6% Ga^{3+}	300–500	0.035 (500 K)	0.83 (500 K)
	$SrZn_{0.33}Nb_{0.67}O_3$:8% Ga^{3+}	300–500	0.032 (500 K)	0.73 (500 K)
Pr^{3+}: $^1D_2 \rightarrow {}^3H_4$, $^3P_0 \rightarrow {}^3F_2$	$SrZn_{0.33}Nb_{0.67}O_3$	300–500	0.007 (500 K)	0.35 (400 K)
	$SrZn_{0.33}Nb_{0.67}O_3$:4% Ga^{3+}	300–500	0.020 (500 K)	0.57 (500 K)
	$SrZn_{0.33}Nb_{0.67}O_3$:6% Ga^{3+}	300–500	0.029 (500 K)	0.70 (500 K)
	$SrZn_{0.33}Nb_{0.67}O_3$:8% Ga^{3+}	300–500	0.026 (500 K)	0.70 (500 K)

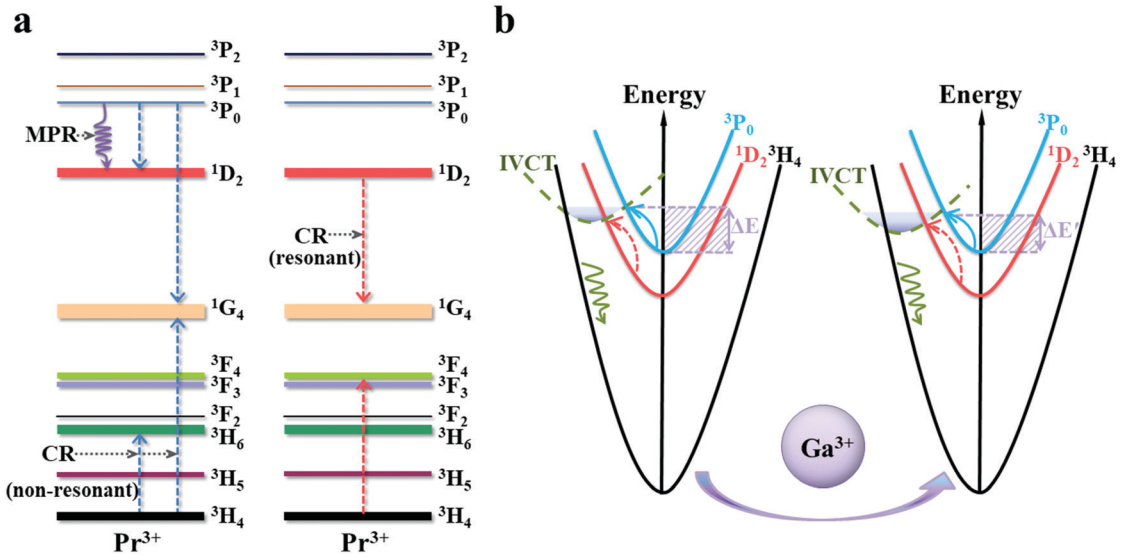

Fig. 8 (a) Schematic energy-transfer diagram for the cross-relaxation and multiphonon relaxation processes of Pr^{3+}. (b) Configurational coordinate diagrams showing the temperature increase-induced non-radiative relaxation processes of Pr^{3+} in $SrZn_{0.33}Nb_{0.67}O_3$ and $SrZn_{0.33}Nb_{0.67}O_3$:Ga^{3+}.

significantly accelerated by elevating the temperature than that of the latter. However, the MPR process has less impact on the depopulation probability of the $^3P_0$ state in niobate due to the large energy gap ($\Delta E \approx 3500$ cm^{-1}) between the $^3P_0$ and $^1D_2$ states according to previous studies.[21] Notably, the low-lying Pr^{3+}–Nb^{5+} IVCT state is regarded as one of the most important depopulation pathways for the $^3P_0$ level in $SrZn_{0.33}Nb_{0.67}O_3$. As illustrated in in Fig. 8(b), both of the $^3P_0$ and $^1D_2$ emissions can be de-excited from Pr^{3+}–Nb^{5+} IVCT with phonons assisting. However, the electrons in the $^1D_2$ state have a higher crossover energy than in $^3P_0$ state, thus leading to the diverse thermal response of the $^3P_0$ and $^1D_2$ emissions. The empirical formula for estimating the IVCT energy in Pr^{3+}-doped niobite is as follows:[37]

$$\mathrm{IVCT}\left(\mathrm{Pr}^{3+}, \mathrm{cm}^{-1}\right) = 58\,800 - 49\,800\frac{\chi_{\mathrm{opt}}\left(\mathrm{Nb}^{5+}\right)}{\mathrm{d}\left(\mathrm{Pr}^{3+} - \mathrm{Nb}^{5+}\right)} \quad (9)$$

where $\chi_{opt}(Nb^{5+})$ represents the electronegativity of Nb^{5+}, and $d(Pr^{3+}$–$Nb^{5+})$ represents the shortest distance between Pr^{3+} and Nb^{5+} in the host. When Ga^{3+} ions are incorporated, the unit cell of $SrZn_{0.33}Nb_{0.67}O_3$ shrinks, as confirmed by the XRD results in Fig. 1(a), which may reduce the distance between Pr^{3+} and Nb^{5+}, consequently resulting in a lower-lying Pr^{3+}–Nb^{5+} IVCT state. Therefore, the energy barrier $\Delta E'$ for the $^3P_0$ state in Ga^{3+} co-doped $SrZn_{0.33}Nb_{0.67}O_3$:Pr^{3+} is smaller than ΔE in $SrZn_{0.33}Nb_{0.67}O_3$:Pr^{3+}. This explains why the doping of Ga^{3+} accelerates the thermal quenching of the blue emission ($^3P_0 \rightarrow {}^3H_4$) and the red emission ($^3P_0 \rightarrow {}^3F_2$). Since the crossover energy from $^1D_2$ to the Pr^{3+}–Nb^{5+} IVCT state is much larger, a small quantity of Ga^{3+} doping has minor influence on the $^1D_2$ emission. Moreover, some of the electrons depopulated from the $^3P_0$ level may relax to the $^1D_2$ level through the Pr^{3+}–Nb^{5+} IVCT bridge. Thus, all these factors together promote the temperature-sensing performance of the designed luminescent thermometer.

It is known that the relative sensitivity S_r is a critical working parameter since it allows the standardization of diverse luminescence-based temperature sensors regardless of the difference in intuitive observations.[1] To further evaluate the temperature-sensing performance of the Ga^{3+},Pr^{3+} co-doped $SrZn_{0.33}Nb_{0.67}O_3$ phosphor, typical Pr^{3+}-activated niobate, zirconate and germanate thermometric phosphors[14,15,21,35–37] reported in recent years are displayed in Table 2 for comparison. As illustrated in the table, the $SrZn_{0.33}Nb_{0.67}O_3$:Pr^{3+},6%

Table 2 Maximum relative sensitivities of representative Pr^{3+}-activated optical temperature-sensing materials in previous reports

Transition	Material	Temperature range (K)	$S_{r\text{-}max}$ (% K^{-1})	Ref.
Pr^{3+}: $^1D_2 \rightarrow {}^3H_4$, $^3P_0 \rightarrow {}^3H_4$	$YNbO_4$	303–543	1.56 (503 K)	17
	$Sr_2(Ge_{0.75}Si_{0.25})O_4$	275–650	0.30 (460 K)	18
	$LaMg_{0.402}Nb_{0.598}O_3$	298–533	0.71 (473 K)	24
	$GdNbO_4$	300–700	0.70 (430 K)	38
	Sr_2GeO_4	300–600	0.60 (300 K)	39
	$La_{0.4}Gd_{1.6}Zr_2O_7$	15–650	0.81 (650 K)	40
	$SrZn_{0.33}Nb_{0.67}O_3$:6% Ga^{3+}	300–500	0.83 (500 K)	This work
Pr^{3+}: $^1D_2 \rightarrow {}^3H_4$, $^3P_0 \rightarrow {}^3F_2$	$LaMg_{0.402}Nb_{0.598}O_3$	298–533	0.73 (473 K)	24
	$SrZn_{0.33}Nb_{0.67}O_3$:6% Ga^{3+}	300–500	0.70 (500 K)	This work

Ga^{3+} in this work has a higher S_r than the zirconate and germanate thermometric phosphors. Moreover, except for $LaMg_{0.402}Nb_{0.598}O_3$:$Pr^{3+}$, there are few investigations on temperature sensitivities based on two-FIR models. Clearly, compared with $LaMg_{0.402}Nb_{0.598}O_3$:$Pr^{3+}$, the $SrZn_{0.33}Nb_{0.67}O_3$:Pr^{3+},6% Ga^{3+} phosphor has made some progress to a certain degree. The analysis above indicates that the obtained $SrZn_{0.33}Nb_{0.67}O_3$:Pr^{3+},Ga^{3+} phosphor could be employed as a promising candidate for self-calibrating temperature measurement.

Conclusion

In summary, $SrZn_{0.33}Nb_{0.67}O_3$ phosphors doped with Pr^{3+},Ga^{3+} were successfully synthetized *via* a high-temperature solid-state reaction route, and the temperature-dependent luminescence of Pr^{3+} is investigated for the first time. Under ultraviolet excitation, the $SrZn_{0.33}Nb_{0.67}O_3$:*x*%Pr (x = 0.25/0.75/1.25/2) phosphors exhibit bright blue and red emissions, which are located at 491 nm, 619 nm and 651 nm. Remarkably, the temperature sensitivities of the FIR thermometer are significantly enhanced when Ga^{3+} is incorporated. Specifically, the maximum absolute and relative sensitivities for the 6% Ga^{3+} co-doped sample are increased five- and two-fold, respectively, compared with the undoped sample. Analysis of the configurational coordinate diagram indicated that the changed thermosensitive properties are ascribed to the intervalence charge transfer state interfered Pr^{3+} luminescence. The results suggest the potential application of the $SrZn_{0.33}Nb_{0.67}O_3$:Pr^{3+},Ga^{3+} phosphor in optical thermometry. In addition, this study offers new thoughts for improving the performance of FIR-based luminescent thermometers.

Conflicts of interest

There are no conflicts to declare.

Acknowledgements

This work was supported by the National Natural Science Foundation of China (52102186), the Guangdong Basic and Applied Basic Research Foundation (2019A1515110801), the Science Foundation for High-level Talents of Wuyi University (2018AL016), the Wuyi University–Macau University Joint Research Fund (2019WGALH08), and the Special projects in key fields of Guangdong Universities (2021ZDZX1022).

References

1 C. Bradac, S. F. Lim, H. C. Chang and I. Aharonovich, Optical Nanoscale Thermometry: From Fundamental Mechanisms to Emerging Practical Applications, *Adv. Opt. Mater.*, 2020, **8**, 2000183.
2 X. D. Wang, O. S. Wolfbeis and R. J. Meier, Luminescent probes and sensors for temperature, *Chem. Soc. Rev.*, 2013, **42**, 7834–7869.
3 D. Parker, J. D. Fradgley and K. L. Wong, The design of responsive luminescent lanthanide probes and sensors, *Chem. Soc. Rev.*, 2021, **50**, 8193–8213.
4 Z. L. Ji, Y. Cheng, X. S. Cui, H. Lin, J. Xu and Y. S. Wang, Heating-induced abnormal increase in Yb^{3+} excited state lifetime and its potential application in lifetime luminescence nanothermometry, *Inorg. Chem. Front.*, 2019, **6**, 110–116.
5 F. Jahanbazi and Y. B. Mao, Recent advances on metal oxide-based luminescence thermometry, *J. Mater. Chem. C*, 2021, **9**, 16410–16439.
6 Y. Y. Tu, S. L. Zhao, D. Y. He, T. Wu, H. Zhang, R. S. Lei, L. H. Huang and S. Q. Xu, A portable all-fiber thermometer based on the fluorescence intensity ratio (FIR) technique in rare earth doped TeO_2–WO_3–La_2O_3–Na_2O glass, *J. Mater. Chem. C*, 2018, **6**, 7063–7069.
7 S. Senapati and K. K. Nanda, Red emitting Eu:ZnO nanorods for highly sensitive fluorescence intensity ratio based optical thermometry, *J. Mater. Chem. C*, 2017, **5**, 1074–1082.
8 J. Zhang, J. J. Chen and Y. I. Zhang, Temperature-sensing luminescent materials $La_{9.67}Si_6O_{26.5}$:Yb^{3+}–Er^{3+}/Ho^{3+} based on pump-power-dependent upconversion luminescence, *Inorg. Chem. Front.*, 2020, **7**, 4892–4901.
9 Z. Sun, M. C. Jia, Y. L. Wei, J. C. Cheng, T. Q. Sheng and Z. L. Fu, Constructing new thermally coupled levels based on different emitting centers for high sensitive optical thermometer, *Chem. Eng. J.*, 2020, **381**, 122654.
10 G. T. Xiang, Q. Xia, X. T. Liu and X. J. Wang, Optical thermometry based on the thermally coupled energy levels of Er^{3+} in the upconversion materials, *Dalton Trans.*, 2020, **49**, 17115–17120.

11 H. Zhang, J. T. Ye, X. L. Wang, S. L. Zhao, R. S. Lei, L. H. Huang and S. Q. Xu, Highly reliable all-fiber temperature sensor based on the fluorescence intensity ratio (FIR) technique in Er^{3+}/Yb^{3+} co-doped $NaYF_4$ phosphors, *J. Mater. Chem. C*, 2019, **7**, 15269–15275.

12 P. Du, X. Y. Huang and J. S. Yu, Yb^{3+}-Concentration dependent upconversion luminescence and temperature sensing behavior in Yb^{3+}/Er^{3+} codoped Gd2MoO6 nanocrystals prepared by a facile citric-assisted sol–gel method, *Inorg. Chem. Front.*, 2017, **4**, 1987–1995.

13 T. Hu, Y. Gao, M. Molokeev, Z. G. Xia and Q. Y. Zhang, Non-stoichiometry in $Ca_2Al_2SiO_7$ enabling mixed-valent europium toward ratiometric temperature sensing, *Sci. China Mater.*, 2019, **62**, 1807–1814.

14 N. Z. Zhang, D. W. Zhang, J. Zhao and Z. G. Xia, Fabrication of dual-emitting dye-encapsulated metal–organic framework as a stable fluorescent sensor for metal ions detection, *Dalton Trans.*, 2019, **48**, 6794–6799.

15 Y. Zhou, D. N. Zhang, J. Zeng, N. Gan and J. Cuan, A luminescent Lanthanide-free MOF nanohybrid for highly sensitive ratiometric temperature sensing in physiological range, *Talanta*, 2018, **181**, 410–415.

16 Q. Wang, M. Liao, Q. M. Lin, M. X. Xiong, X. Zhang, H. F. Dong, Z. P. Lin, M. R. Wen, D. Y. Zhu, Z. F. Mu and F. G. Wu, The design of dual-switch fluorescence intensity ratio thermometry with high sensitivity and thermochromism based on a combination strategy of intervalence charge transfer and up-conversion fluorescence thermal enhancement, *Dalton Trans.*, 2021, **50**, 9298–9309.

17 Y. Gao, F. Huang, H. Lin, J. Xu and Y. S. Wang, Intervalence charge transfer state interfered Pr^{3+} luminescence: A novel strategy for high sensitive optical thermometry, *Sens. Actuators, B*, 2017, **243**, 137–143.

18 M. Sójka, J. F. C. B. Ramalho, C. D. S. Brites, K. Fiaczyk, L. D. Carlos and E. Zych, Bandgap Engineering and Excitation Energy Alteration to Manage Luminescence Thermometer Performance. The Case of $Sr_2(Ge,Si)O_4:Pr^{3+}$, *Adv. Opt. Mater.*, 2019, **7**, 1901102.

19 M. Sójka, C. D. S. Brites, L. D. Carlos and E. Zych, Exploiting bandgap engineering to finely control dual-mode $Lu_2(Ge,Si)O_5:Pr^{3+}$ luminescence thermometers, *J. Mater. Chem. C*, 2020, **8**, 10086–10097.

20 Y. Gao, F. Huang, H. Lin, J. G. Zhou, J. Xu and Y. S. Wang, A Novel Optical Thermometry Strategy Based on Diverse Thermal Response from Two Intervalence Charge Transfer States, *Adv. Funct. Mater.*, 2016, **26**, 3139–3145.

21 W. Tang, Y. Sun, S. C. Wang, B. S. Du, Y. Q. Yin, X. Liu, B. Yang, W. W. Cao and M. Yu, Pr^{3+}-Doped $(K_{0.5}Na_{0.5})NbO_3$ as a high response optical oxygen sensing agent, *J. Mater. Chem. C*, 2016, **4**, 11508–11513.

22 R. Shi, L. T. Lin, P. Dorenbos and H. B. Liang, Development of a potential optical thermometric material through photoluminescence of Pr^{3+} in La_2MgTiO_6, *J. Mater. Chem. C*, 2017, **5**, 10737–10745.

23 Y. J. Wang, V. Tsiumra, Q. Peng, H. B. Liang, Y. Zhydachevskyy, M. Chaika, P. Dluzewski, H. Przybylinska and A. Suchocki, Hole Trapping Process and Highly Sensitive Ratiometric Thermometry over a Wide Temperature Range in Pr^{3+}-Doped $Na_2La_2Ti_3O_{10}$ Layered Perovskite Microcrystals, *J. Phys. Chem. A*, 2019, **123**, 4021–4033.

24 H. Zhang, Z. Gao, G. G. Li, Y. L. Zhu, S. Q. Liu, K. Li and Y. J. Liang, A ratiometric optical thermometer with multicolor emission and high sensitivity based on double perovskite $LaMg_{0.402}Nb_{0.598}O_3$: Pr^{3+} thermochromic phosphors, *Chem. Eng. J.*, 2020, **380**, 122491.

25 X. H. Li, L. Zhou, M. D. Dramićanin, Q. Tang, X. P. Jing, J. X. Shi, Y. Q. Xu and M. M. Wu, Broad-band emission of $A_3B'B''_2O_9$ complex perovskites (A = Ba, Sr; B′ = Zn; B″ = Ta, Nb) realized by structural variations of the B site order–disorder, *J. Mater. Chem. C*, 2018, **6**, 12566–12574.

26 W. Y. Li, L. X. Ning and P. A. Tanner, Double perovskite structure: a vibrational and luminescence investigation providing a perspective on crystal field strength, *J. Phys. Chem. A*, 2012, **116**, 7337–7344.

27 A. F. Fuentes, O. Hernández-Ibarra, G. Mendoza-Suarez, J. I. Escalante-Garcıa, K. Boulahya and U. Amador, Structural analysis of several W(VI) and Mo(VI) complex perovskites prepared by the polymeric precursors method, *J. Solid State Chem.*, 2003, **173**, 319–327.

28 S. Sinha, M. K. Mahata, H. C. Swart, A. Kumar and K. Kumar, Enhancement of upconversion, temperature sensing and cathodoluminescence in the K^+/Na^+ compensated $CaMoO_4:Er^{3+}/Yb^{3+}$ nanophosphor, *New J. Chem.*, 2017, **41**, 5362–5372.

29 N. An, H. L. Zhou, K. S. Zhu, L. H. Ye, J. R. Qiu and L.-G. Wang, Improved temperature sensing performance of $YAG:Ho^{3+}/Yb^{3+}$ by doping Ce^{3+} ions based on up-conversion luminescence, *J. Alloys Compd.*, 2020, **843**, 156057.

30 M. Wang, R. Wang, Y. Li, N. Lin and Y. Xu, The enhancement mechanism of $Yb^{3+}/Tm^{3+}/12CaO{\cdot}7Al_2O_3$ *via* Li^+ incorporation and temperature sensing applications, *Mate. Today Chem.*, 2019, **14**, 100187.

31 M. L. Zhang, X. S. Zhai, P. P. Lei, S. Yao, X. Xu, L. L. Dong, K. M. Du, C. Y. Li, J. Feng and H. J. Zhang, Selective enhancement of green upconversion luminescence from $NaYF_4$:Yb, Er microparticles through Ga^{3+} doping for sensitive temperature sensing, *J. Lumin.*, 2019, **215**, 116632.

32 L. Kong, Y. Y. Liu, L. P. Dong, L. Zhang, L. Qiao, W. S. Wang and H. P. You, Enhanced red luminescence in $CaAl_{12}O_{19}:Mn^{4+}$ via doping Ga^{3+} for plant growth lighting, *Dalton Trans.*, 2020, **49**, 1947–1954.

33 W. Yan, S. G. Xiao and X. L. Yang, Novel red-emitting phosphor $Li_2MgZrO_4:Mn^{4+}$, Ga^{3+} for warm white LEDs based on blue-emitting chip, *RSC Adv.*, 2019, **9**, 5354–5361.

34 X. A. Chen, Y. An and W. Q. Xiao, A new solid solution $Bi_{1.48}Eu_{0.52}Pb_{0.5}Sr_{0.5}B_2O_7$ and luminescent properties of the $Bi_{2-x}Pb_{0.5}Sr_{0.5}B_2O_7$:$xEu^{3+}$ phosphors, *J. Lumin.*, 2021, **237**, 118137.

35 Y. Gao, Y. Cheng, T. Hu, Z. L. Ji, H. Lin, J. Xu and Y. S. Wang, Broadening the valid temperature range of optical thermometry through dual-mode design, *J. Mater. Chem. C*, 2018, **6**, 11178–11183.

36 S. X. Wang, S. W. Ma, J. M. Wu, Z. M. Ye and X. Cheng, A promising temperature sensing strategy based on highly

sensitive Pr^{3+}-doped $SrRE_2O_4$ (RE = Sc, Lu and Y) luminescent thermometers, *Chem. Eng. J.*, 2020, **393**, 124564.

37 C. M. Liu, F. J. Pan, Q. Peng, W. J. Zhou, R. Shi, L. Zhou, J. H. Zhang, J. Chen and H. B. Liang, Excitation Wavelength Dependent Luminescence of $LuNbO_4$:Pr^{3+}—Influences of Intervalence Charge Transfer and Host Sensitization, *J. Phys. Chem. C*, 2016, **120**, 26044–26053.

38 W. G. Ye, C. Y. Ma, Y. B. Li, C. Zhao, Y. Z. Wang, Y. Z. Zuo, C. D. Zou, Z. C. Wen, Y. K. Li, X. Y. Yuan and Y. G. Cao, Anti-Thermal-Quenching Red-Emitting $GdNbO_4$:Pr^{3+} Phosphors Based on Metal-to-Metal Charge Transfer for Optical Thermometry Application, *J. Mater. Chem. C*, 2021, **42**, 15201–15211.

39 C. D. S. Brites, K. Fiaczyk, J. F. C. B. Ramalho, M. Sójka, L. D. Carlos and E. Zych, Widening the Temperature Range of Luminescent Thermometers through the Intra- and Interconfigurational Transitions of Pr^{3+}, *Adv. Opt. Mater.*, 2018, **6**, 1701318.

40 J. Trojan-Piegza, C. D. S. Brites, J. F. C. B. Ramalho, Z. J. Wang, G. H. Zhou, S. W. Wang, L. D. Carlos and E. Zych, $La_{0.4}Gd_{1.6}Zr_2O_7$:0.1%Pr transparent sintered ceramic – a wide-range luminescence thermometer, *J. Mater. Chem. C*, 2020, **8**, 7005–7011.